ADVANCED FUNCTIONAL MATERIALS
www.afm-journal.de

Ternary Ta_2NiSe_5 Flakes for a High-Performance Infrared Photodetector

*Liang Li, Weike Wang, Lin Gan, Nan Zhou, Xiangde Zhu, Qi Zhang, Huiqiao Li, Mingliang Tian, and Tianyou Zhai**

Multielemental systems enable the use of multiple degrees of freedom for control of physical properties by means of stoichiometric variation. This has attracted extremely high interest in the field of 2D optoelectronics in recent years. Here, for the first time, multilayer 2D ternary Ta_2NiSe_5 flakes are successfully fabricated using a mechanical exfoliation method from chemical vapor transport synthesized high quality bulk and the optoelectronic properties are systematically investigated. Importantly, a high responsivity of 17.21 A W^{-1} and high external quantum efficiency of 2645% are recorded from an as-fabricated photodetector at room temperature in air; this is superior to most other 2D materials-based photodetectors that have been reported. More intriguingly, a usual sublinear and an unusual superlinear light-intensity-dependent photocurrent are observed under air and vacuum, respectively. These excellent and special properties make multilayer ternary Ta_2NiSe_5 a highly competitive candidate for future infrared optoelectronic applications and an interesting platform for photophysics studies.

1. Introduction

Infrared (IR) photodetectors have wide applications in many filed including military communication, medical and environmental monitoring, remote control, and thermal imaging[1–4] and have attracted increasing attention in recent years. In the past decades, numerous IR photodetectors have been fabricated based on traditional narrow-bandgap materials, such as InAs, InSb, HgZnTe, and HgCdTe.[5] However, not to mention the toxicity of these materials, the bulk lattice structure of these semiconductors makes them difficult in monolithic integration and fabrication flexible devices applications in near future.[4] 2D materials have layered structure, which renders them great advantages in the applications of monolithic integration, flexible devices, and even wearables.[4,6,7] Interestingly, the electron structure of 2D semiconductors is usually related to the number of layers and external strain, providing simple ways to tune the optoelectronic properties just by changing the number of layers or strain engineering.[7] Motivated by these, a large number of 2D materials such as graphene,[8,9] GeSe,[10] SnS_2,[11] MoS_2,[12,13] black phosphorus,[4,14] $ReSe_2$,[15,16] and MoS_2/black phosphorus heterojunction[17] have been attempted in IR photodetectors. However, only the very recently reported (3-aminopropyl) triethoxysilane (APTES) and triphenylphosphine (PPh_3) treated $ReSe_2$ IR detector exhibited a high performance with photoresponsivity of about 10^4 A W^{-1} and switch time of about 50 ms,[15] most IR photodetectors are still suffering from drawbacks such as low responsivity,[8,9,14] slow response,[8,9] and environmental instability.[4,14,17]

Ternary Ta_2NiSe_5 is a layered material stacked by weak van der Waals interaction.[18] The structure can be characterized as a series of zigzag wave chains (**Figure 1**a), in which $[TaSe_6]_2$ dimer chains that composed by two $[TaSe_6]$ octahedral single chains interconnect with $NiSe_4$ tetrahedral single chains, are periodically assembled.[18,19] This distorted chain structure makes a considerable anisotropic electrical behavior expected within the layer plane.[20] Especially, bulk Ta_2NiSe_5 is a direct bangap semiconductor (E_g = 0.36 eV),[20,21] unlike most transition metal dichalcogenides (TMDs) undergone an indirect-to-direct bandgap transition when scaled down to monolayer,[22] Ta_2NiSe_5 will maintain its direct bandgap nature.[23] This unique robust electronic character makes Ta_2NiSe_5 an ideally candidate for those applications in which high carrier concentration and large light adsorption efficiency are simultaneously demanded. Moreover, Ta_2NiSe_5 will experience a second-order phase transition at a critical temperature of 328 K.[24,25] Below this temperture, anomalous flattening and broadening of the valence-band occur, which indicates the existing of excitonic insulator (EI) ground state.[24] The direct bandgap nature combined with the EI phase offers an unprecedented opportunity to directly study the effect of photoexcitation when electronic states implicated in the exciton formation.[26] As for 2D Ta_2NiSe_5 material fabrication, only the work of ultrathin flakes

Dr. L. Li, Dr. L. Gan, N. Zhou, Dr. Q. Zhang, Dr. H. Q. Li, Prof. T. Y. Zhai
State Key Laboratory of Material Processing and Die and Mould Technology
School of Materials Science and Engineering
Huazhong University of Science and Technology (HUST)
Wuhan 430074, P. R. China
E-mail: zhaity@hust.edu.cn
Dr. W. K. Wang, Dr. X. D. Zhu, Prof. M. L. Tian
High Magnetic Field Laboratory
Chinese Academy of Science
Hefei 230031, P. R. China

DOI: 10.1002/adfm.201603804

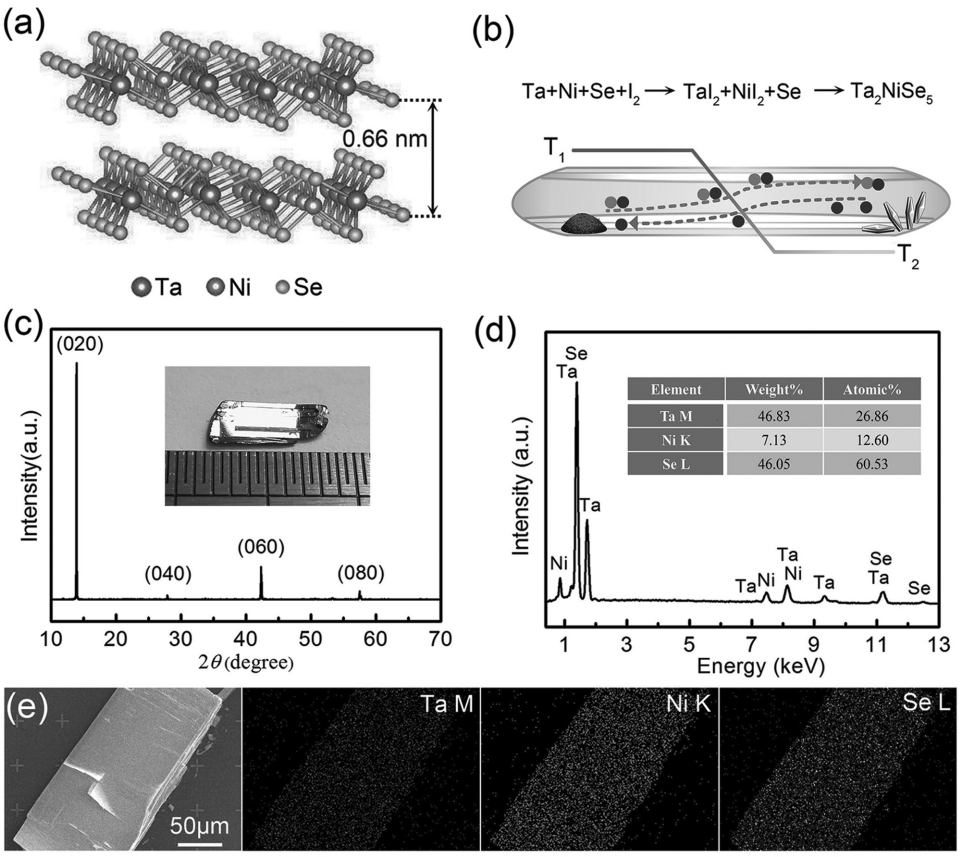

Figure 1. Synthesis and characterization of Ta_2NiSe_5 single crystals. a) Structural model of layered Ta_2NiSe_5. b) Schematic diagram of CVT process. c) XRD pattern of layered Ta_2NiSe_5 crystal, inset: the optical image of Ta_2NiSe_5 single crystal. d) EDX result of Ta_2NiSe_5 single crystal. e) SEM image and EDS elemental mapping of an exfoliated Ta_2NiSe_5 microflake.

has been reported recently, in which Ta_2NiSe_5 nanosheets are acquired with high yield by liquid exfoliation method.[19] However, the merit of high yield of liquid exfoliation method is degraded by the drawbacks by small size (typically several hundred nanometers in length) and low quality of products, which hinders the studies and applications of samples for electronics and optoelectronics.[27,28] Considering the unique robust moderate direct bandgap of Ta_2NiSe_5,[20,21] we speculate it will be a promising candidate for IR photodetectors of excellent responsivity. Compared to single elemental or binary systems,[29–33] ternary systems have more degrees of freedom to tune the electronic or optoelectronic properties of systems just by means of stoichiometric variation.[34–38]

Herein, multilayer ternary chalcogenide Ta_2NiSe_5 flakes are successfully exfoliated via mechanical exfoliation method from chemical vapor transport (CVT) synthesized single crystalline bulk; moreover, their optoelectronic properties have been systematically studied as well. An excellent IR photoresponsivity of 17.21 A W^{-1} and high external quantum efficiency (EQE) of 2645% in air are collected from Ta_2NiSe_5 flakes-based IR photodetector, superior to most of other reported 2D materials-based IR photodetectors. More interestingly, a usual sublinear and an unusual superlinear light intensity dependence of photocurrent under air and vacuum have been observed, respectively, which could be attributed to the combined effect of adsorbents and different types of recombination centers in our samples. The excellent and special photoelectronic properties make Ta_2NiSe_5 a promising active 2D material for future application in optoelectronics and an interesting platform for photophysics study.

2. Results and Discussion

The 3D structural model of Ta_2NiSe_5 crystal shown in Figure 1a clearly stresses the layered nature and Van Der Waals interaction among single layers. In addition, the distance between adjacent layers is ≈0.66 nm.[18,19] The top view of the Ta_2NiSe_5 crystal is shown in Figure S1 (Supporting Information). The Ta_2NiSe_5 crystals have been synthesized via CVT in the two-zone furnace which is schematically shown in Figure 1b, and the synthesis details could be found in the Experimental Section. Figure 1c shows powder X-ray diffraction (XRD) pattern of Ta_2NiSe_5 crystal. All peaks can be identified to the monoclinic space group C2/*c* (15) (JCPDS PDF No. 01-078-0279). The strong diffraction peak at about 13.8° can be indexed to the (020) plane, while other relatively smaller periodic diffraction reflections located at about 27.8°, 42.3°, and 57.5° are assigned to the (040), (060), and (080) planes, respectively. The predominance peak demonstrates that these Ta_2NiSe_5 single crystals (the inset in Figure 1c) have a highly preferential

Adv. Funct. Mater. **2016**,
DOI: 10.1002/adfm.201603804

orientation along the [020] direction. The energy-dispersive X-ray spectroscopy (EDS) spectrum of a Ta_2NiSe_5 single crystal shown in Figure 1d gives strong signals of Ta, Ni, and Se, and agrees well with the stoichiometric of Ta_2NiSe_5. Figure 1e shows the scanning electron microscopy (SEM) image and EDS elemental mapping of an exfoliated Ta_2NiSe_5 microflake. These results reveal a layered structure and a uniform spatial distribution of Ta, Ni, and Se of our synthesized sample.

Moreover, the X-ray photoelectron spectroscopy (XPS) was also used to characterize Ta_2NiSe_5 crystal sample, as shown in Figure S2 (Supporting Information). The whole XPS spectrum of Ta_2NiSe_5 demonstrated in Figure S2a (Supporting Information) clearly identified the signals of elements of Ta, Ni, and Se. The fitted peaks located around 23.4 and 25.7 eV of Ta 4f spectrum shown in Figure S2b (Supporting Information) can be indexed to the core level peaks of Ta $4f^{7/2}$ and Ta $4f^{5/2}$.[24] Besides, the two fitted peaks at 853.8 and 861.7 eV of Ni 2p spectrum exhibited in Figure S2c (Supporting Information) represent the binding energies of Ni^{2+} in Ta_2NiSe_5,[19,24] while three peaks fitted at 53.3, 54.2, and 55.4 eV of Se 3d spectrum displayed in Figure S2d (Supporting Information) are ascribed to Se^{2-} of Ta_2NiSe_5.[19,24]

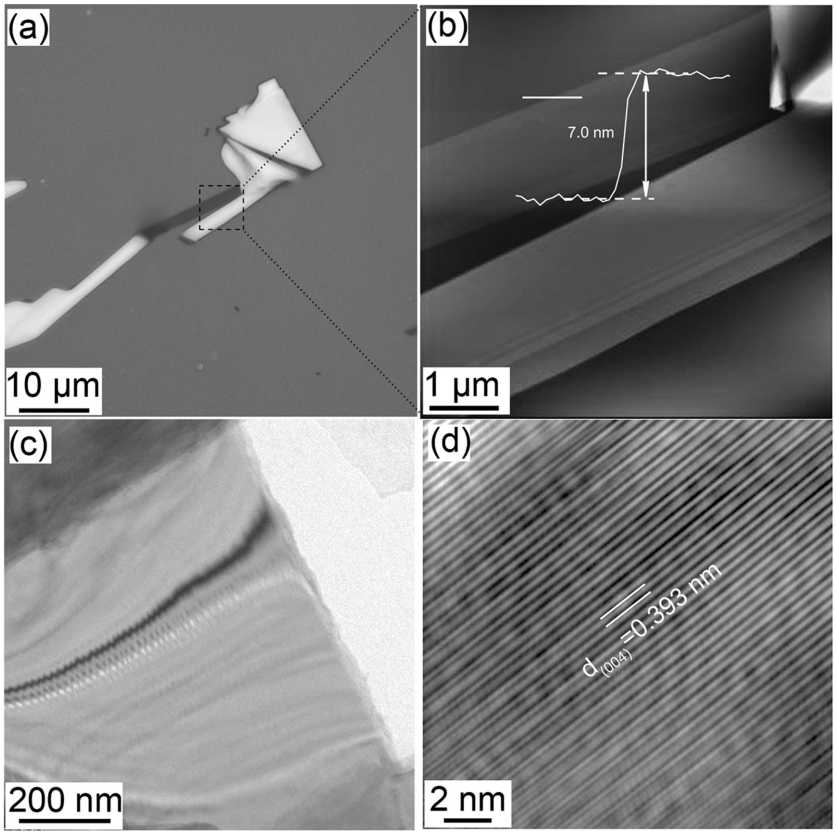

Figure 2. a) Optical microscopy photograph and b) the corresponding AFM topography of typical exfoliated Ta_2NiSe_5 flakes. c) TEM and d) HRTEM of an exfoliated sample.

Compared with chemical vapor deposition or liquid exfoliation method, 2D flakes prepared by mechanical exfoliation always have clean surface, pristine state, and high-quality structures.[39] Here, through this simple scotch tape-based exfoliation method, we achieved multilayer Ta_2NiSe_5 flakes, details can be found in the Experimental Section. The optical microscope photograph of typical mechanical exfoliated Ta_2NiSe_5 flakes is shown in **Figure 2**a, from which one can see that the length of the dark section is up to 15 μm, much larger than the liquid exfoliated counterpart.[19] The corresponding atomic force microscopy (AFM) image in Figure 2b confirms the thickness is ≈7 nm (about ten layers). Figure 2c shows the low magnitude transmission electron microscopy (TEM) image of a typical mechanical exfoliated Ta_2NiSe_5 flake. The corresponding high-resolution TEM (HRTEM) image presented in Figure 2d exhibits a clear and sharp lattice fringe with an interplanar distance of 0.393 nm, corresponding to the (004) planes, further confirming the single-crystalline nature.

To determine the optoelectronic properties of multilayer Ta_2NiSe_5, photodetectors based on exfoliated Ta_2NiSe_5 flakes are fabricated using standard electron-beam lithography (EBL). Here, if not specially noted, the photoelectronic measurements were taken under excitation of 808 nm laser. **Figure 3** summarizes the optoelectronic properties of a multilayer Ta_2NiSe_5 photodetector under air condition. The multilayer Ta_2NiSe_5-based IR photodetector is schematically shown in Figure 3a, where Cr/Au top electrodes were patterned via thermal evaporation. Figure 3b exhibits the comparison of *I–V* relationship under dark condition and under laser illumination with different power intensities. The inset shows the AFM image of the device in which one can see that the thickness of Ta_2NiSe_5 flake is ≈9.4 nm and the separation between two Cr/Au electrodes is about 4.9 μm. Note that all *I–V* curves exhibit nearly linear behavior, indicating a good Ohmic contact between Ta_2NiSe_5 flake and Cr/Au electrodes. The slopes of the *I–V* curves increased with increasing power density, suggesting the power density-dependent photocurrent relationship. To further investigate this relationship, we measured the time-dependent photoresponse using different power densities range from 94 to 838 mV cm^{-1}, as shown in Figure 3c. Then, we can plot the dependent curve of photocurrent I_{ph} ($I_{ph} = I_{illumination} - I_{dark}$) versus incident laser intensity (P), as exhibited in Figure 3d, in which one can see that the I_{ph} is proportional to P^{β} with a fitting value $\beta = 0.98$. This value is less than 1, but very close to 1, showing a sublinear behavior. We also measured the wavelength dependent photocurrent spectrum for the photodetector (see Figure S3, Supporting Information), which clearly reveals a wide photoresponse range. The cyclability of the photodetector is checked under power intensity of 481 mW cm^{-1} ($V_{bias} = 0.1$ V) by artificially switching on/off the incident light at an interval of 20 s. Several cycles were performed and the result was shown in Figure 3e, from which one can achieved that there is little deviation during cycles, revealing the photoresponse of the detector is reversible and

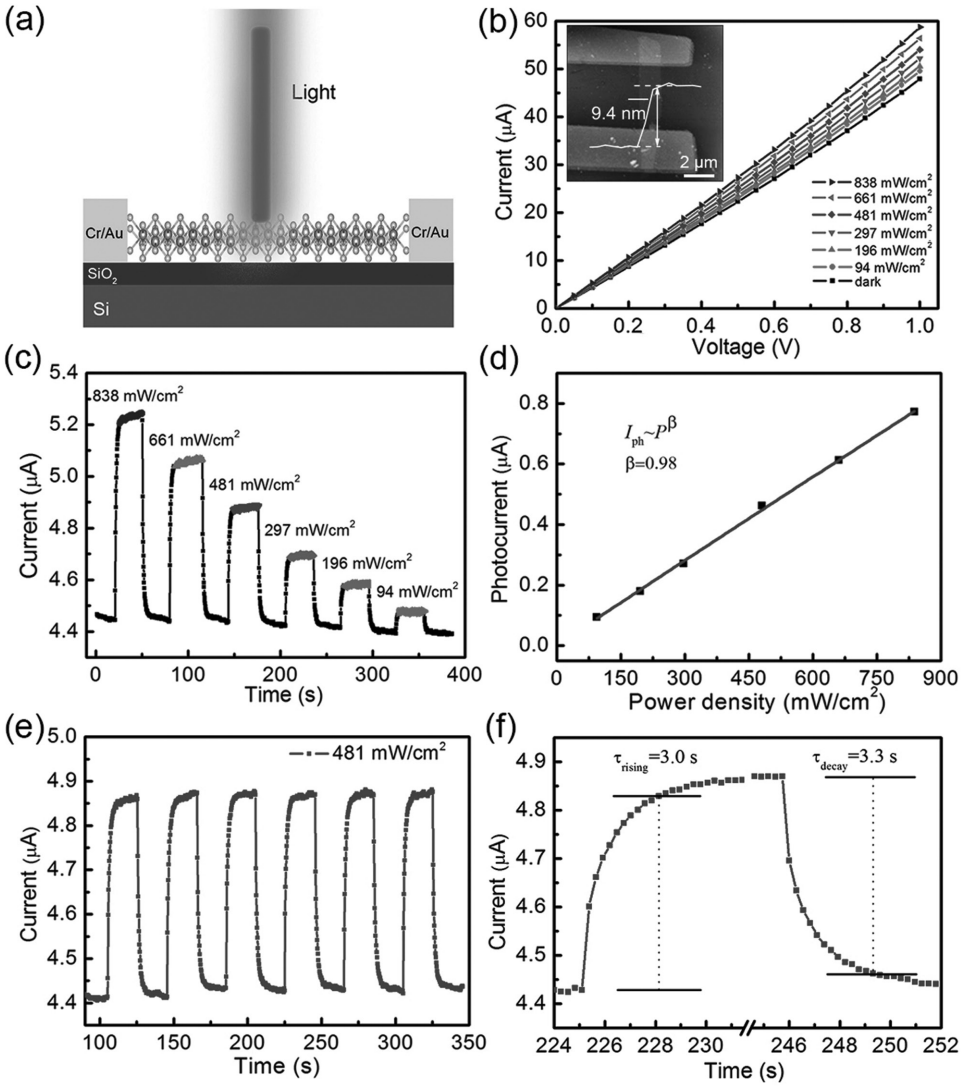

Figure 3. Optoelectronic properties of multilayer Ta_2NiSe_5 photodetector in air. a) A schematic image of the photodetector. b) *I–V* curves of the device in the dark and under illumination with different intensities, inset: the AFM image of the detector. c) Light intensity-dependent photoresponse at V_{bias} = 0.1 V. d) Photocurrent as a function of laser power intensity. e) Time-resolved photoresponse of the device recorded for a power density of 481 mW cm^{-1}. f) Response rate of photodetector acquired from one magnified circle of response with rising time 3.0 s and decay time 3.3 s.

stable. Figure 3f described the magnified plot of one circle of Figure 3e, the rising time (τ_{rising}) and decay time (τ_{decay}) are 3.0 and 3.3 s, respectively. The switching speed is slower than APTES and PPh_3 treated $ReSe_2$ photodetector[15] but is comparable or faster than many other reported 2D IR detectors (e.g., about 10^2 for graphene nanoribbons, monolayer graphene and bilayer MoS_2).[8,9,12] Future improvement of switch time might be obtained by O_2 plasma treatment according to the literature.[40] The persistent photoconductivity as in Figure 3f is well known to produce due to charge trap[41] and could be eliminated by making photo thin-film transistor using gate pulse voltage after illumination stopped.[42–44]

Besides response rate, the responsivity (R_λ) and EQE are other two crucial parameters to evaluate the sensitivity of photodetectors.[2,7,45–48] Responsivity can be defined as, $R_\lambda = I_{ph}/PS$, where I_{ph} is the photogenerated current, P is the power intensity of the laser, and S is the effective irradiated area of the flake. In our study, the S is 5.58 μm^2 and I_{ph} is 0.46 μA under power intensity of 481 mW cm^{-2} at V_{bias} = 0.1 V, thus, the calculated responsivity is 17.21 A W^{-1}. Such a value is about two orders of magnitude higher than monolayer graphene and few layers black phosphorus.[9,14] Afterward, the EQE can be calculated according to EQE = $hcR_\lambda/e\lambda$, where h, c, λ, and e are the Plank's constant, velocity of light, exciting wavelength, and elementary electronic charge, respectively. The calculated value of EQE is 2645%. The values of photoresponsivity and EQE of our device are superior to many other reported 2D-based IR detectors as summarized in **Table 1**, suggesting that Ta_2NiSe_5 flakes are promising in the applications of infrared photodetection. The photoelectronic properties were also performance on two other different thicknesses flakes, and are shown in Figure S4 (Supporting Information). The thicker device exhibits a much higher photocurrent and higher responsivity, which can be contributed to the relatively weaker scattering and higher light

DOI: 10.1002/adfm.201603804

Table 1. Comparison in the performance of IR potodetectors based on multilayer Ta_2NiSe_5 and some previously reported 2D materials.

Materials	Wavelength [nm]	External bias [V]	R_λ [A W^{-1}]	EQE [%]	Switching time [s]	Reference
Graphene nanoribbons	1550	2	1	80	≈10^2	[8]
Monolayer graphene	1470	0.02	0.2	–	≈10^2	[9]
Few layers black phosphorus	≈1550	2	0.657	–	–	[14]
GeSe nanosheet	808	4	≈3.5	≈530	0.1	[10]
SnS_2 nanosheets	850	5	9.2×10^{-4}	0.15		[11]
Bilayer MoS_2	1070	0.8	5.2	–	≈10^2	[12]
Multilayer MoS_2	850	1	9×10^{-5}	–	–	[13]
Multilayer Ta_2NiSe_5	808	0.1	17.21	2645	$\tau_{rising} = 3.0$, $\tau_{decay} = 3.3$	This work

absorbability.[40] Thus, the thickness control is very important for future applications.

In order to investigate the photoconductive mechanism, the photoelelectronic measurements of the device were also performed under vacuum (≈10^{-4} Torr) condition. **Figure 4**a,b shows the *I–V* characteristics of the photodetector under dark and laser illumination in different atmospheres, respectively. One can see that both the dark current and illumination current in vacuum are higher than that in air. Figure 4c shows the several cycles of time-dependent photoresponse in vacuum under 0.1 V bias. The dark current and illumination current in vacuum are 4.45 and 8.14 μA, respectively, which are both higher than that in air (see Figure 3e, I_{dark} = 4.41 μA and $I_{illumination}$ = 4.87 μA). As shown in Figure 4d, the response rate in vacuum are 34.3 and 33.3 s for rising and decay, respectively, which are much slower than that obtained in air (see Figure 3f, τ_{rising} = 3.0 s and τ_{decay} = 3.3 s). In short, the photocurrent in vacuum is larger than that in ambient while the response rate in vacuum is much slower. This phenomenon supports the well-accepted effect of oxygen chemisorption on the photosensitivity.[48–52] Field effect transistor measurement descripted in Figure S5 (Supporting Information) confirmed the Ta_2NiSe_5 is n-type, suggesting the conductivity depends mainly on electrons. In air condition, oxygen molecules adsorbed onto the surface of the multilayer Ta_2NiSe_5, captured free electrons from the flake, in agreement with the scheme [$O_2(g) + e^- \rightarrow O_2^-$ (ad)], which creates a depletion layer near the surface, resulting in low conductivity in the dark state.[49,50,52] When exposed to laser with energy larger than the band gap, electron–hole pairs are generated, and the holes migrate to the surface and combine with O_2^- through [$h^+ + O_2^-$ (ad) $\rightarrow O_2$ (g)], resulting in an increasement of electron concentration, which further lead to the photocurrent enhancement.[10,49,52] When in vacuum, the electrons of negatively O_2^- return to the depletion layer on the flake surface, leading to increase of the carrier lifetime,[48] so the current is higher in vacuum than that in air. In addition, the longer carrier lifetime makes a longer recombination time, causing a slower response rate in vacuum. Figure 4e shows the light intensity-dependent photoresponse under vacuum condition. As expected, the photocurrent increase with increasing power density. More importantly, the saturation platform of photocurrent is growing even steeper with increasing power density, which means it may take more time for achieving photocurrent saturation under higher intensity, such interesting phenomenon will be discussed below. Figure 4f illustrates the intensity dependent photocurrent under vacuum, two points should be noted: one is that the exponent β in air ($\beta = 0.98$) is smaller than that under vacuum ($\beta = 1.1$); the other is that the exponent β is larger than 1, showing a superlinear behavior. The first phenomenon is normal which reflects that the recombination probability of photoexcited carriers could be increased due to the existing of adsorbates in air, causing the fall in responsivity.[53] However, the later one is unusual, which will be discussed below.

The most interesting finding which has not well explained is summarized here: the fitting exponent β of intensity dependence of photocurrent in air is less than 1, showing a sublinear behavior; while in vacuum, the value of β is larger than 1, exhibiting a superlinear behavior. We assume that both hole-trapping on the surface due to the oxygen adsorption and desorption and the existence of different types of recombination centers which will be discussed below contribute to the above-mentioned phenomenon. In vacuum, the adsorbents are lack, the presence of different recombination centers contribute to the superlinear phenomenon.[54,55] To explain the superlinear behavior of Ta_2NiSe_5 in vacuum, we present a model as descript in **Figure 5**. For simplicity, three types of recombination centers (RCs, the existence of in-gap states due to selenium vacancy or defect may act as recombination centers[9,56–58]) with different energies and capture cross-sections are presented. RC_1, RC_2, and RC_3 are located near the valence, mid-, and conduction band, respectively, here, RC_1 have a low electron capture cross-section but a high hole capture cross-section, while RC_2 and RC_3 have both large holes and electrons capture cross-sections. Under dark, the Fermi level (E_F) is located above RC_1 and RC_2, but below RC_3. When illuminated by light, the hole and electron concentrations are augmented, leading the Quasi-Fermi levels E_F^p and E_F^n move apart. At low intensity, the RC_1 and RC_2 are mostly occupied, while the RC_3 are mostly empty, and the recombination rate is dominated by RC_3. With increasing the power density, the occupancy ratio of RC_1 and RC_2 decrease, while occupancy ratio of RC_3 increase. When the intensity is high enough, the density of empty RC_1, RC_2, and RC_3 are comparable, resulting in the huge drops of recombination rate, further leading to the superlinear. The existence of different types of recombination centers have also been used to explain the

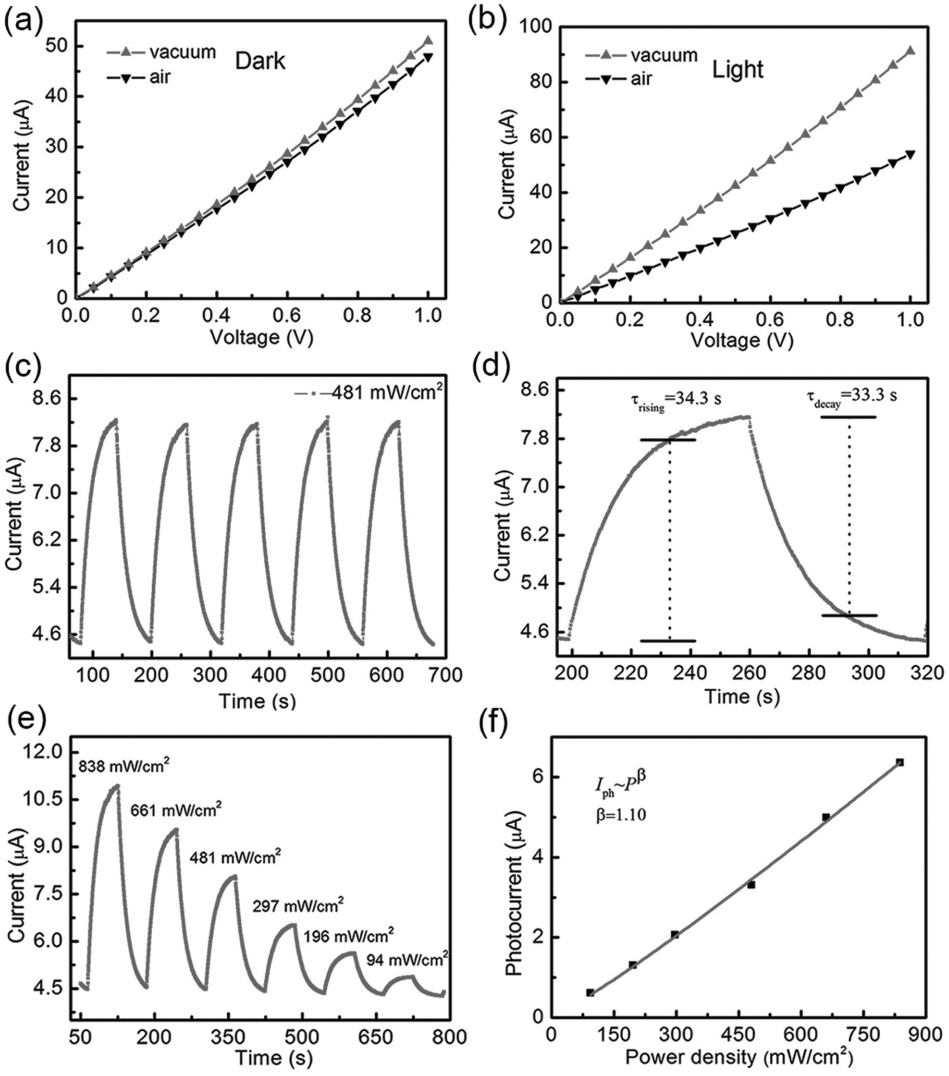

Figure 4. *I–V* characteristics under a) dark and b) laser illumination in air and vacuum. c) Time-dependent responses of the photodetector in vacuum at V_{bias} = 0.1 V recorded for a power density of 481 mW cm^{-1}. d) Response rate of photodetector acquired from one magnified circle in (c) with rising time 34.3 s and decay time 33.3 s. e) Light intensity-dependent photoresponse under vacuum. f) Photocurrent as a function of laser power intensity under vacuum.

superlinear behavior in $MoS_{2(1-x)}Se_{2x}$.[55] Moreover, the steeper and steeper saturation platform of photocurrent with increasing power density shown in Figure 4e indicate the recombination rate drops with intensity, confirming our deduction. Such superlinear behavior also has been observed in graphene and MoS_2 photodetectors.[9,53] When in air, the adsorbents contribution is increased. At higher intensities, the number of available hole-traps present at the surface is dramatically reduced, leading to the subliear behavior.[52] In short, the adsorbents and different types of recombination centers should take responsibility for the sublinear and superlinear of light intensity-dependent photocurrent, respectively. In air, the impact from the adsorbents is larger than recombination centers, leading to sublinear; while in vacuum, the contribution from recombination centers is greater, causing superlinear behavior.

To understand in depth the photoelectronic performance of multilayer Ta_2NiSe_5, we further investigated the electrotransport and photoresponse at varies temperatures. Here, all measurements are performed under vacuum of ≈10^{-4} Torr. **Figure 6**a shows the typical *I–V* curves of the Ta_2NiSe_5 device at varies temperature, it can be seen that all the curves exhibit nearly linear behavior, suggesting good Ohmic contact at all temperatures. The temperature dependence resistance of the device is shown in Figure 6b, as can be seen, the resistance decreases with increasing temperature, showing a typical semiconductor behavior, similar to the literature.[25] Furthermore, the activation energy calculated from the fitting curves of ln$R$ versus $1/T$ is 257 meV, which fits the narrow band-gap nature of Ta_2NiSe_5.[18] Figure 6c shows the normalized time-resolved photoresponse at various temperatures, from which one can obviously obtained that the photoresponse of the detector dependent strongly on the temperature, that is, the photoresponse decrease as the temperature increase. The in-gap states which have discussed above may be responsible for this phenomenon. More detailed,

Adv. Funct. Mater. **2016**,
DOI: 10.1002/adfm.201603804

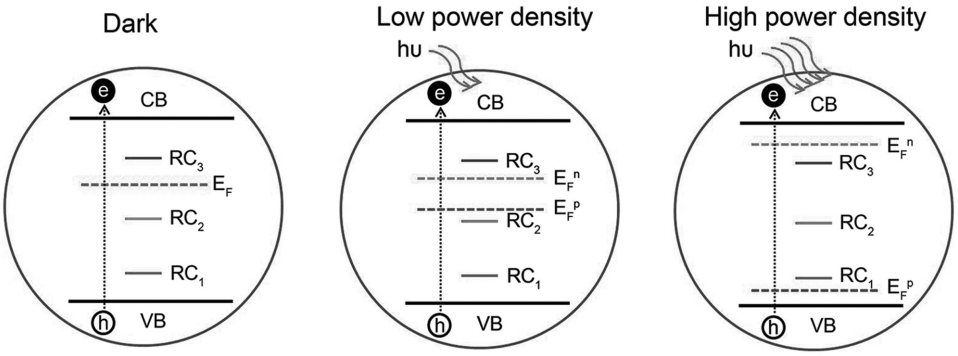

Figure 5. Schematic to explain the behavior of superlinear photocurrent. Bandgap model with three different types of recombination centers (RCs) under dark (left image), low (centered image), and high (right image) power density illuminated conditions. E_F is the Fermi level, E_F^n and E_F^p are the quasi Fermi levels of electrons and holes under illumination, respectively.

the recombination speed of captured electrons in the in-gap states will be faster with the increase of temperature, therefore, the photoresponse reduced.[9] As descripted in Figure 6d, the on/off ratio continuously increases from 1.85 to 62.22 as the temperature decrease from 300 to 20 K. The increase of on/off ratio can be explained by the strongly suppressed of dark current at low temperature as is shown in Figure 6d.[59]

3. Conclusion

We for the first time have successfully isolated high quality multilayer flakes of ternary Ta_2NiSe_5 from corresponding bulk crystal via mechanical exfoliation technique from CVT synthesized single crystalline bulk and fabricated IR photodetectors based on as-isolated samples. A high responsivity of 17.21 A W^{-1} and outstanding EQE of 2645% at room temperature in air condition are collected, which is superior to most of reported other 2D materials-based photodetectors. In addition, we observed a normal sublinear and an abnormal superlinear illumination intensity dependence of photocurrent under air and vacuum, respectively. We assume that the combined effect of adsorbents and different types of recombination centers should take responsibility for such interesting phenomenon. Moreover, low temperature study reveal that the photoresponse of IR photodetectors decrease with temperature increase. Our finding not

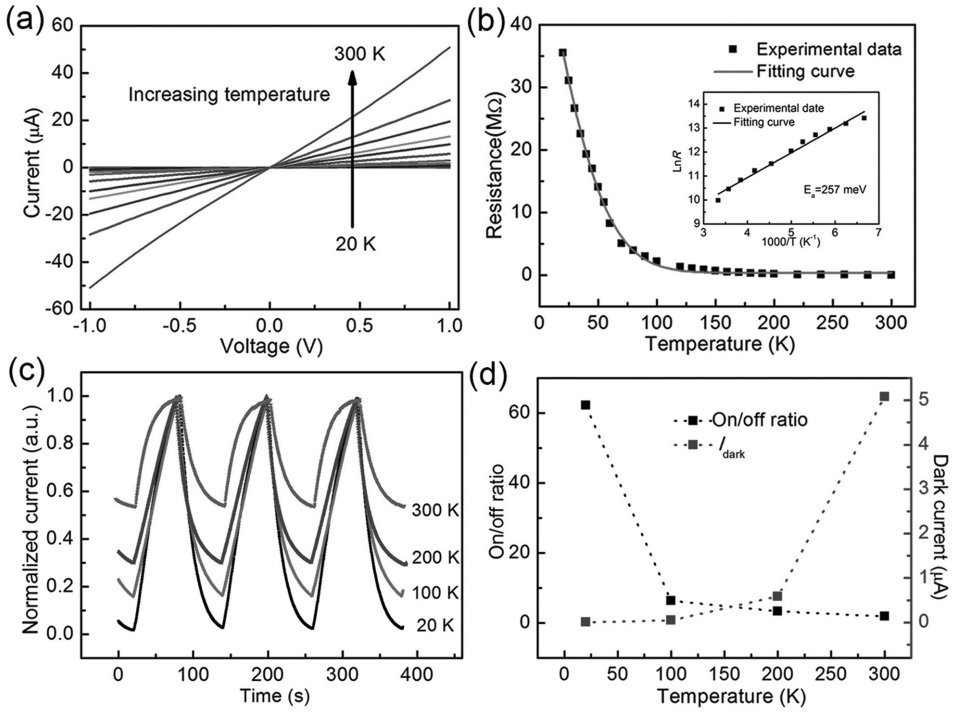

Figure 6. a) *I–V* curves of the device at different temperatures in vacuum. b) Temperature dependence resistance of multilayer Ta_2NiSe_5, inset: ln*R* as the function of 1000/*T*. c) Normalized time-resolved photoresponse at various temperatures recorded for a power density of 481 mW cm^{-1}. d) On/off ratio and I_{dark} at different temperatures.

only suggests that layered Ta_2NiSe_5 is a very promising ternary material for the development of 2D optoelectronic device, but also provide a platform to explore novel photophysics regarding the unusual superlinear behavior.

4. Experimental Section

Synthesis of Ta_2NiSe_5 Single Crystals: High-quality Ta_2NiSe_5 single crystals were prepared by the CVT method using iodine as a transport agent in a horizontal two-zone furnace. 1 g starting materials of high-purity Ta, Ni, and Se powders (≥99.9%, Alfa) were mixed stoichiometrically and ground thoroughly, then vacuum sealed (>10^{-4} Torr) into a quartz tube with some additional iodine (10 mg cm^{-3}). The tube was slowly heated up to 850 °C on one end while the other end was kept at 800 °C. After 10 d of growth, shiny crystals with strip-like shape were obtained, with typical dimensions of $10 \times 3 \times 0.2$ mm^3.

Mechanical Exfoliation: Multilayer Ta_2NiSe_5 flakes were isolated from the corresponding bulk crystals and then transferred onto the freshly cleaned Si wafer containing a 300 nm thick SiO_2 dielectric layer. An optical microscope (Olympus, BX51) equipped with a charge-coupled device (Olympus, DP73) was used to examine the flakes. The thickness of the Ta_2NiSe_5 flakes was first roughly evaluated from different interference color using the optical microscope and then precisely determined by AFM.

Characterization: The XRD patterns were collected with a Rigaku-TTR3 X-ray diffractometer using Cu-Kα radiation at room temperature in the 2θ range of 10°–70° with a scan step width of 0.02°. The composition and elements distribution of as-fabricated microflake was determined by energy dispersive X-ray spectroscopy (EDX) attached to the SEM (FEI Helios Nanolab 600i). XPS was performed on a Thermo Fisher VG ESCALAB 250 instrument using Al Kα as X-ray source. The transmission electron microscopy (TEM) and HRTEM was applied on JEM-2100(HR) to investigate the microstructure of the exfoliated samples. The thickness measurements of the exfoliated flakes were carried out with AFM (SPM9700).

Device Fabrication and Measurements: The photodetector devices were fabricated by standard EBL and deposited Cr/Au (10 nm/40 nm) as contact electrodes using thermal evaporation (Nexdep, Angstrom Engineering). The electronic and photoelectronic measurements were performed by a probe station (CRX-6.5K, Lake Shore) equipped with a semiconductor characterization system (4200SCS, Keithley). An 808 nm laser with tunable power was used to measure the photoresponse of the devices.

Supporting Information

Supporting Information is available from the Wiley Online Library or from the author.

Acknowledgements

L.L. and W.K.W. contributed equally to this work. This work was supported by National Basic Research Program of China (21322106, 51472097, and 21501060), National Key Research and Development Program of "Strategic Advanced Electronic Materials" (2016YFB0401100), National Basic Research Foundation of China (2015CB932600), Program for HUST Interdisciplinary Innovation Team (2015ZDTD038), and the Fundamental Research Funds for the Central University. The authors also want to thank Analytical and Testing Center in Huazhong University of Science and Technology for the technical support. In particular, L.L. thanks Dr. P. L. Gong from South University of Science and Technology of China (SUSTC) for the helpful discussions.

Received: July 26, 2016
Revised: August 31, 2016
Published online:

[1] X. Gong, M. Tong, Y. Xia, W. Cai, J. S. Moon, Y. Cao, G. Yu, C. L. Shieh, B. Nilsson, A. J. Heeger, *Science* **2009**, *325*, 1665.
[2] X. Zhou, G. Lin, Q. Zhang, X. Xiong, H. Li, J. Han, T. Zhai, *J. Mater. Chem. C* **2016**, *4*, 2111.
[3] L.-H. Zeng, M.-Z. Wang, H. Hu, B. Nie, Y.-Q. Yu, C.-Y. Wu, L. Wang, J.-G. Hu, C. Xie, F.-X. Liang, L.-B. Luo, *ACS Appl. Mater. Interfaces* **2013**, *5*, 9362.
[4] Q. Guo, A. Pospischil, M. Bhuiyan, H. Jiang, H. Tian, D. Farmer, B. Deng, C. Li, S. J. Han, H. Wang, Q. Xia, T. P. Ma, T. Mueller, F. Xia, *Nano Lett.* **2016**, *16*, 4648.
[5] A. Rogalski, *Infrared Phys. Technol.* **2002**, *43*, 187.
[6] M. Razeghi, B.-M. Nguyen, *Rep. Prog. Phys.* **2014**, *77*, 082401.
[7] M. Buscema, J. O. Island, D. J. Groenendijk, S. I. Blanter, G. A. Steele, H. S. van der Zant, A. Castellanos-Gomez, *Chem. Soc. Rev.* **2015**, *44*, 3691.
[8] B. Chitara, L. Panchakarla, S. Krupanidhi, C. Rao, *Adv. Mater.* **2011**, *23*, 5419.
[9] Y. Zhang, T. Liu, B. Meng, X. Li, G. Liang, X. Hu, Q. J. Wang, *Nat. Commun.* **2013**, *4*, 1811.
[10] B. Mukherjee, Y. Cai, H. R. Tan, Y. P. Feng, E. S. Tok, C. H. Sow, *ACS Appl. Mater. Interfaces* **2013**, *5*, 9594.
[11] J.-J. Wu, Y.-R. Tao, Y. Wu, X.-C. Wu, *Sens. Actuators, B* **2016**, *231*, 211.
[12] W. Wang, A. Klots, D. Prasai, Y. Yang, K. I. Bolotin, J. Valentine, *Nano Lett.* **2015**, *15*, 7440.
[13] W. Choi, M. Y. Cho, A. Konar, J. H. Lee, G. B. Cha, S. C. Hong, S. Kim, J. Kim, D. Jena, J. Joo, S. Kim, *Adv. Mater.* **2012**, *24*, 5832.
[14] N. Youngblood, C. Chen, S. J. Koester, M. Li, *Nat. Photonics* **2015**, *9*, 247.
[15] S. H. Jo, H. Y. Park, D. H. Kang, J. Shim, J. Jeon, S. Choi, M. Kim, Y. Park, J. Lee, Y. J. Song, *Adv. Mater.* **2016**, *28*, 6711.
[16] M. Hafeez, L. Gan, H. Li, Y. Ma, T. Zhai, *Adv. Mater.* **2016**, DOI: 10.1002/adma.201601977.
[17] L. Ye, H. Li, Z. Chen, J. Xu, *ACS Photonics* **2016**, *3*, 692.
[18] S. A. Sunshine, J. A. Ibers, *Inorg. Chem.* **1985**, *24*, 3611.
[19] C. Tan, P. Yu, Y. Hu, J. Chen, Y. Huang, Y. Cai, Z. Luo, B. Li, Q. Lu, L. Wang, Z. Liu, H. Zhang, *J. Am. Chem. Soc.* **2015**, *137*, 10430.
[20] F. Di Salvo, C. Chen, R. Fleming, J. Waszczak, R. Dunn, S. Sunshine, J. A. Ibers, *J. Less-Common Met.* **1986**, *116*, 51.
[21] E. Canadell, M. H. Whangbo, *Inorg. Chem.* **1987**, *26*, 3974.
[22] Q. H. Wang, K. Kalantar-Zadeh, A. Kis, J. N. Coleman, M. S. Strano, *Nat. Nanotechnol.* **2012**, *7*, 699.
[23] S. Y. Kim, Y. Kim, C.-J. Kang, E.-S. An, H. K. Kim, M. J. Eom, M. Lee, C. Park, T. H. Kim, H. C. Choi, *ACS Nano* **2016**, DOI: 10.1021/acsnano.6b04796.
[24] Y. Wakisaka, T. Sudayama, K. Takubo, T. Mizokawa, M. Arita, H. Namatame, M. Taniguchi, N. Katayama, M. Nohara, H. Takagi, *Phys. Rev. Lett.* **2009**, *103*, 026402.
[25] K. Seki, Y. Wakisaka, T. Kaneko, T. Toriyama, T. Konishi, T. Sudayama, N. Saini, M. Arita, H. Namatame, M. Taniguchi, *Phys. Rev. B* **2014**, *90*, 155116.
[26] S. Mor, M. Herzog, D. Golež, P. Werner, M. Eckstein, N. Katayama, M. Nohara, H. Takagi, T. Mizokawa, C. Monney, *arXiv preprint arXiv:1608.05586* **2016**.
[27] J. H. Lee, D. W. Shin, V. G. Makotchenko, A. S. Nazarov, V. E. Fedorov, Y. H. Kim, J. Y. Choi, J. M. Kim, J. B. Yoo, *Adv. Mater.* **2009**, *21*, 4383.
[28] X. Huang, Z. Zeng, H. Zhang, *Chem. Soc. Rev.* **2013**, *42*, 1934.
[29] M. Huang, M. Wang, C. Chen, Z. Ma, X. Li, J. Han, Y. Wu, *Adv. Mater.* **2016**, *28*, 3481.
[30] X. Zhou, L. Gan, W. Tian, Q. Zhang, S. Jin, H. Li, Y. Bando, D. Golberg, T. Zhai, *Adv. Mater.* **2015**, *27*, 8035.
[31] Y. Ma, *Sci. Bull.* **2015**, *20*, 1789.
[32] M. Hafeez, L. Gan, H. Li, Y. Ma, T. Zhai, *Adv. Funct. Mater.* **2016**, *26*, 4551.

[33] P. Yu, X. Yu, W. Lu, H. Lin, L. Sun, K. Du, F. Liu, W. Fu, Q. Zeng, Z. Shen, C. Jin, Q. Wang, Z. Liu, *Adv. Funct. Mater.* **2016**, *26*, 137.
[34] S. Lei, A. Sobhani, F. Wen, A. George, Q. Wang, Y. Huang, P. Dong, B. Li, S. Najmaei, J. Bellah, G. Gupta, A. D. Mohite, L. Ge, J. Lou, N. J. Halas, R. Vajtai, P. Ajayan, *Adv. Mater.* **2014**, *26*, 7666.
[35] H. Li, X. Duan, X. Wu, X. Zhuang, H. Zhou, Q. Zhang, X. Zhu, W. Hu, P. Ren, P. Guo, L. Ma, X. Fan, X. Wang, J. Xu, A. Pan, X. Duan, *J. Am. Chem. Soc.* **2014**, *136*, 3756.
[36] Q. Ma, M. Isarraraz, C. S. Wang, E. Preciado, V. Klee, S. Bobek, K. Yamaguchi, E. Li, P. M. Odenthal, A. Nguyen, *ACS Nano* **2014**, *8*, 4672.
[37] P. Perumal, R. K. Ulaganathan, R. Sankar, Y. M. Liao, T. M. Sun, M. W. Chu, F. C. Chou, Y. T. Chen, M. H. Shih, Y. F. Chen, *Adv. Funct. Mater.* **2016**, *26*, 3630.
[38] C. Tan, W. Zhao, A. Chaturvedi, Z. Fei, Z. Zeng, J. Chen, Y. Huang, P. Ercius, Z. Luo, X. Qi, B. Chen, Z. Lai, B. Li, X. Zhang, J. Yang, Y. Zong, C. Jin, H. Zheng, C. Kloc, H. Zhang, *Small* **2016**, *12*, 1866.
[39] H. Li, J. Wu, Z. Yin, H. Zhang, *Acc. Chem. Res.* **2014**, *47*, 1067.
[40] J. Shim, A. Oh, D. H. Kang, S. Oh, S. K. Jang, J. Jeon, M. H. Jeon, M. Kim, C. Choi, J. Lee, *Adv. Mater.* **2016**, *28*, 6985.
[41] X. Dang, C. Wang, E. Yu, K. Boutros, J. Redwing, *Appl. Phys. Lett.* **1998**, *72*, 2745.
[42] S. Jeon, S.-E. Ahn, I. Song, C. J. Kim, U.-I. Chung, E. Lee, I. Yoo, A. Nathan, S. Lee, K. Ghaffarzadeh, *Nat. Mater.* **2012**, *11*, 301.
[43] S. E. Ahn, I. Song, S. Jeon, Y. W. Jeon, Y. Kim, C. Kim, B. Ryu, J. H. Lee, A. Nathan, S. Lee, *Adv. Mater.* **2012**, *24*, 2631.
[44] S. Jeon, I. Song, S. Lee, B. Ryu, S. E. Ahn, E. Lee, Y. Kim, A. Nathan, J. Robertson, U. I. Chung, *Adv. Mater.* **2014**, *26*, 7102.
[45] T. Zhai, L. Li, Y. Ma, M. Liao, X. Wang, X. Fang, J. Yao, Y. Bando, D. Golberg, *Chem. Soc. Rev.* **2011**, *40*, 2986.
[46] S. C. Dhanabalan, J. S. Ponraj, H. Zhang, Q. Bao, *Nanoscale* **2016**, *8*, 6410.
[47] W. Tian, H. Lu, L. Li, *Nano Res.* **2015**, *8*, 382.
[48] H. Liu, Z. Zhang, L. Hu, N. Gao, L. Sang, M. Liao, R. Ma, F. Xu, X. Fang, *Adv. Opt. Mater.* **2014**, *2*, 771.
[49] H. Kind, H. Yan, B. Messer, M. Law, P. Yang, *Adv. Mater.* **2002**, *14*, 158.
[50] T. Zhai, L. Li, X. Wang, X. Fang, Y. Bando, D. Golberg, *Adv. Funct. Mater.* **2010**, *20*, 4233.
[51] Y. Tao, X. Wu, W. Wang, J. Wang, *J. Mater. Chem. C* **2015**, *3*, 1347.
[52] C. Soci, A. Zhang, B. Xiang, S. A. Dayeh, D. Aplin, J. Park, X. Bao, Y.-H. Lo, D. Wang, *Nano Lett.* **2007**, *7*, 1003.
[53] W. Zhang, J. K. Huang, C. H. Chen, Y. H. Chang, Y. J. Cheng, L. J. Li, *Adv. Mater.* **2013**, *25*, 3456.
[54] A. Rose, *Phys. Rev.* **1955**, *97*, 322.
[55] V. Klee, E. Preciado, D. Barroso, A. E. Nguyen, C. Lee, K. J. Erickson, M. Triplett, B. Davis, I.-H. Lu, S. Bobek, *Nano Lett.* **2015**, *15*, 2612.
[56] D. Kim, D.-H. Kim, J.-H. Lee, J. C. Grossman, *Phys. Rev. Lett.* **2013**, *110*, 196802.
[57] D. Kufer, G. Konstantatos, *Nano Lett.* **2015**, *15*, 7307.
[58] Y. Zhang, D. Zherebetskyy, N. D. Bronstein, S. Barja, L. Lichtenstein, D. Schuppisser, L.-W. Wang, A. P. Alivisatos, M. Salmeron, *Nano Lett.* **2015**, *15*, 3249.
[59] Q. Wang, Y. Wen, F. Yao, Y. Huang, Z. Wang, M. Li, X. Zhan, K. Xu, F. Wang, F. Wang, J. Li, K. Liu, C. Jiang, F. Liu, J. He, *Small* **2015**, *11*, 5388.